The effects of collision energy, vibrational mode, and vibrational angular momentum on energy transfer and dissociation in NO_2^+–rare gas collisions: An experimental and trajectory study

Jianbo Liu, Brady W. Uselman, Jason M. Boyle, et al.

View Online   Export Citation

ARTICLES YOU MAY BE INTERESTED IN

The effects of collision energy, vibrational mode, and vibrational angular momentum on energy transfer and dissociation in NO_2^+–rare gas collisions: An experimental and trajectory study

Jianbo Liu, Brady W. Uselman, Jason M. Boyle, and Scott L. Anderson[a)]
Department of Chemistry, University of Utah, Salt Lake City, Utah 84112-0850

A combined experimental and trajectory study of vibrationally state-selected NO_2^+ collisions with Ne, Ar, Kr, and Xe is presented. Ne, Ar, and Kr are similar in that only dissociation to the excited singlet oxygen channel is observed; however, the appearance energies vary by ~4 eV between the three rare gases, and the variation is nonmonotonic in rare gas mass. Xe behaves quite differently, allowing efficient access to the ground triplet state dissociation channel. For all four rare gases there are strong effects of NO_2^+ vibrational excitation that extend over the entire collision energy range, implying that vibration influences the efficiency of collision to internal energy conversion. Bending excitation is more efficient than stretching; however, bending angular momentum partially counters the enhancement. Direct dynamics trajectories for NO_2^+ + Kr reproduce both the collision energy and vibrational state effects observed experimentally and reveal that intracomplex charge transfer is critical for the efficient energy transfer needed to drive dissociation. The strong vibrational effects can be rationalized in terms of bending, and to a lesser extent, stretching distortion enhancing transition to the Kr^+–NO_2 charge state. © *2006 American Institute of Physics.*
[DOI: 10.1063/1.2229207]

I. INTRODUCTION

Collisional energy transfer, i.e., inelastic scattering, is an important and ubiquitous process. For ion-molecule systems, little is known about the effects of reactant vibrational or rotational excitation on collisional energy transfer, but such information is important for several reasons. Vibrationally excited ions may react quite differently than ground state ions; thus collisional excitation and deexcitation may influence chemistry in plasmas, planetary atmospheres, and molecular clouds. The by far most common type of ion inelastic scattering experiment is collision-induced dissociation (CID), where the near-threshold behavior of the dissociation cross section (σ_{CID}) is modeled to extract dissociation energies. Two assumptions are typically made. The most important is that there is significant probability for collisions where 100% of collision energy (E_{col}) is converted to whatever form of internal energy ($E_{internal}$) is needed to drive dissociation. Only if this assumption is true does σ_{CID} extrapolate to the desired dissociation threshold energy. For typical ion sources, polyatomic reactant ions may have significant vibrational excitation; thus some assumption must also be made regarding the relative efficiency of vibrational energy (E_{vib}) in driving CID, relative to other forms of energy.

Here, we present a study of NO_2^+ excitation and dissociation in collisions with Ne, Ar, Kr, and Xe over the E_{col} range up to 11 eV (i.e., approximately four times the dissociation energy). Experimental results are given for NO_2^+ in its ground state, with one quantum of symmetric stretch excitation and with two quanta of bend excitation, with and with-

out bending angular momentum. Dissociation probability is found to depend strongly and mode specifically on vibration, and even the bending angular momentum state has a significant effect. The validity of the assumptions discussed above varies considerably among the rare gases. In order to help interpret the experimental dissociation behavior and to gain insight into energy transfer, we carried out a quasiclassical trajectory (QCT) study of NO_2^+ + Kr collisions at E_{col} = 8.0 and 9.0 eV, including NO_2^+ vibrational effects. A more limited study of NO_2^+ + Ne collisions at E_{col} = 6.0 and 9.0 eV was done for comparison purposes. In addition to revealing a surprising CID mechanism, these results provide a test of QCT applicability to vibrational dynamics and to a system where two charge states come into play.

II. METHODOLOGY

A. Experiment

The experiments were done using a guided-ion-beam tandem mass spectrometer, described previously, along with the experimental and data analysis protocols.[1–4] Vibrationally state-selected NO_2^+ was generated using a two-color, three photon resonance-enhanced multiphoton ionization (REMPI) scheme, based on a more elaborate REMPI scheme developed by Bell *et al.*[5] In brief, supersonically cooled NO_2 is excited by $\omega_1 + \omega_2$ to a specific vibrational level of the $E\ ^2\Sigma_u^+(3p\sigma)$ intermediate state (ω_1 = 23 097 cm^{-1}, ω_2 = 32 527 – 34 885 cm^{-1}). Ionization occurs with a final photon of either ω_1 or ω_2, producing NO_2^+ with vibrational state purity better than 96%.[6] For this study, NO_2^+ was prepared in its ground state (0,0,0), with one quantum in the symmetric

[a)]Electronic mail: anderson@chem.utah.edu

stretch $[(1,0,0)=170 \text{ meV}]$ or with two quanta of bend excitation. This bend overtone level can be prepared with either zero or two quanta of bending angular momentum $[(0,2^0,0)=155 \text{ meV}; (0,2^2,0)=153 \text{ meV}]$.

A pulsed molecular beam of NO_2 was seeded with He at a 1:5 ratio and skimmed before being introduced to the ionization region. The ionization region is just inside the end of a radio frequency (rf) quadrupole ion guide that focuses the ions into a quadrupole mass filter, which, for this system, is also just operated as an ion guide. Time-of-flight (TOF) gating is used to remove NO^+ fragment ions and clean up the temporal and kinetic energy distributions of the NO_2^+ reactant beam. Ions are injected into an eight-pole rf ion guide, that guides them through a scattering cell filled with the rare gas of interest to 2×10^{-4} Torr. The bias on the injection ion lens is kept positive relative to the ion guide, in order to reflect backscattered NO^+ product ions, so that they can be detected (see below). The guide collects undissociated NO_2^+ together with product ions and passes them into a second, longer guide segment for TOF velocity analysis. Finally, the ions are mass analyzed and counted. The ion kinetic energy distribution ($\Delta KE \sim 0.15$ eV) was measured by TOF, as was the axial velocity distributions for the NO^+ CID product. The data presented are averages of several complete data sets, and the error bars shown are standard deviations. In each set, cross sections were measured for the four NO_2^+ vibrational states and for all four rare gases, in order to minimize the relative uncertainty in comparing different states or target gases.

B. Computational details

Quasiclassical, direct dynamics trajectories were calculated using the general chemical dynamics program VENUS99 of Hase *et al.*[7] to set up the trajectory initial conditions and the Hessian-based method of Bakken *et al.*,[8] implemented in GAUSSIAN03 (revision C.01),[9] to propagate each trajectory, with Hessians recalculated every five steps. The integrations were performed with a step size of ~ 0.4 fs, which conserved total energy to better than 10^{-4} hartree. Because millions of gradient and Hessian evaluations are required, the level of *ab initio* theory used was necessarily modest. The B3LYP method with LanL2DZ basis set was chosen because this combination best fits "benchmark" single point calculations at the QCISD(T)/cc-pVDZ level of theory. The NO_2^+–Kr interaction is largely repulsive, with only a very shallow (~ 0.1 eV) electrostatic well at ~ 3.5 Å center-of-mass separation—negligible relative to the high collision energies simulated. The repulsive wall is slightly softer for B3LYP/LanL2DZ compared to that for QCISD(T)/cc-pVDZ, amounting to a shift of 0.1 Å in the classical turning point. The B3LYP dissociation energy for NO_2^+ [5.11 eV for NO^+ $+O(^1D)$] is slightly higher than the experimental value (4.82 eV);[10] however, as described below, the method used to select "dissociative" trajectories should compensate for the high B3LYP dissociation energy.

Initial conditions were chosen[11] to mimic the conditions used in our experimental study of NO_2^++Kr collisions. Because our experiments generated NO_2^+ by REMPI of a supersonic molecular beam, a 50 K Boltzmann distribution was sampled to generate the NO_2^+ initial rotational motion. The initial vibrational state was simulated by giving the atoms in NO_2^+ kinetic energies and displacements from equilibrium that are appropriate to the desired vibrational state (including zero point energy). We simulated collisions for NO_2^+ in its ground state, with one quantum of symmetric stretch (1,0,0) and with two quanta of the bend. Because the experiments showed the largest effect from the bend overtone level with no bending angular momentum, we chose to simulate the $(0,2^0,0)$ state. Trajectories were started with center-of-mass NO_2^+–Kr separation of 8.0 Å, at which point the interreactant interaction is negligible.

The collision energy E_{col} was set to either 8.0 or 9.0 eV, and orientation and vibrational phases were chosen randomly. For each collision energy and vibrational state, trajectories were run at seven discrete values of the impact parameter (b), ranging from 0.1 to 2.5 Å, allowing us to examine the b dependence of the scattering dynamics. A batch of 300 trajectories was run for each combination of E_{col}, vibrational state, and initial impact parameter. In addition to the Kr trajectories, a more limited set was run for NO_2^++Ne at 6.0 and 9.0 eV collision energies. All trajectories were run for the singlet state of $(NO_2+Rg)^+$, because there is no experimental evidence of triplet production for Kr or Ne. The time for one trajectory varied from 3 to 7 h on Athlon 64 3800+ CPUs; thus the set of 15 000 trajectories required about nine CPU years. For visualization and analysis of individual trajectories, we use the program GOPENMOL.[12] Detailed analysis of individual trajectories and statistical analysis of the trajectory ensemble are done with programs written for this purpose, as described previously.[13,14]

There are two issues with the trajectory methodology for this system. In QCT calculations, vibration is not quantized; thus zero point energy (ZPE) is not conserved. It is possible, therefore, to have trajectories where the final E_{vib} is below the zero point level. Fortunately, such unphysical collisions are negligible because the available energy is much greater than the ZPE. For the same reason, quantization effects are not expected to be large. This issue has been discussed by Miller *et al.*[15] and Untch *et al.*,[16] and QCT simulations have been used successfully to study collisional excitation and CID for a number of systems.[13,17,18] Another issue with QCT is whether anharmonic coupling might lead to spurious vibrational mode scrambling prior to collision. We examined the NO_2^+ vibrational motion over a time scale five times larger than the reactant approach time and found no significant changes in the character of the vibrational motion (i.e., maximum bending angle, and maximum and minimum NO bond lengths). In the final analysis, the important test is how well the trajectories reproduce experiment, and as shown below, the agreement is excellent.
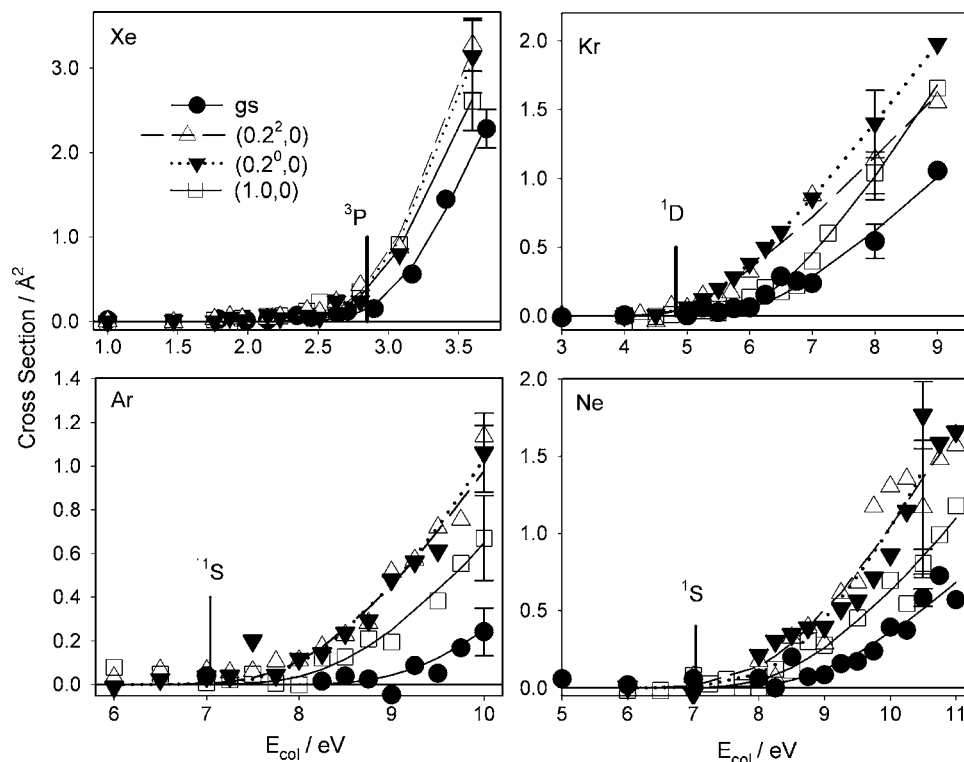
FIG. 1. Integral cross sections for CID of NO$_2^+$ in different initial vibrational states. Labeled vertical lines indicate asymptotic energies for production of NO$^+$ in concert with different O atom states. Points are experimental data, and smooth curves are fits as discussed in the text.

III. EXPERIMENTAL RESULTS

A. Integral cross sections and vibrational effects

The only product ion observed for any of the rare gases was NO$^+$, which is not surprising given its relatively low ionization energy compared to the rare gases. Figure 1 shows the integral cross sections for NO$^+$ production in the near-threshold E_{col} ranges for each rare gas and for NO$_2^+$ in its $(0,0,0)$, $(0,2^0,0)$, $(0,2^2,0)$, and $(1,0,0)$ vibrational states. The symbols are the actual experimental data, and the smooth curves are fits used to account for E_{col} broadening from the distributions of ion beam and target velocities. The fits are based on a modified line-of-centers model cross section, with two adjustable parameters: the "true" threshold energy (E_0) and a parameter (n) that controls the curvature of the cross section near threshold.[19,20] For Xe, a full fitting study was done to address the issue of E_{col} and vibrational effects on the threshold behavior. For Kr, Ar, and Ne, both σ and $d\sigma/dE_{col}$ are small; thus the experimental scatter results in poorly constrained fit parameters. Because our primary interest is in comparing threshold behavior for the different rare gases and vibrational states, we generated a consistent set of fits, by fixing the n parameter at the value (1.8) that gives the best fits for Xe, leaving E_0 as the only adjustable parameter. The resulting E_0 values should be considered to be appearance energies for NO$^+$, corrected for experimental broadening. Making this correction is important, however, because the E_{col} distribution width varies with both E_{col} and rare gas, due to Doppler broadening.[21]

Figure 1 also indicates the energies of various possible CID product channels as vertical lines, labeled as follows:

$$NO_2^+(^1\Sigma_g^+) + Rg(^1S) \rightarrow NO^+(^1\Sigma) + Rg(^1S) + O(^3P),$$

$$\Delta H^0 = 2.85 \text{ eV} \quad (\text{labeled } ^3P),$$

$$\rightarrow NO^+(^1\Sigma) + Rg(^1S) + O(^1D),$$

$$\Delta H^0 = 4.82 \text{ eV} \quad (\text{labeled } ^1D),$$

$$\rightarrow NO^+(^1\Sigma) + Rg(^1S) + O(^1S),$$

$$\Delta H^0 = 7.04 \text{ eV} \quad (\text{labeled } ^1S).$$

Note that for Xe, dissociation is observed at the ^3P dissociation limit, even though this channel is spin forbidden. For all other rare gases, dissociation is not observed until E_{col} exceeds the spin-allowed ^1D limit. For Kr, NO$^+$ signal first becomes significant ~0.7 eV above the ^1D limit, and for Ar and Ne, dissociation is not significant until E_{col} is 3–4 eV above this limit. For Ar and Ne, CID starts near the ^1S limit; however, because ground state NO$_2^+$ correlates to the ^1D limit, the near match is probably coincidental. The appearance energies for CID with Ar are higher than those for Ne, indicating less efficient conversion of E_{col} to drive dissociation. As noted, in addition to the CID channels, NO$^+$ can be produced in concert with RgO:

$$NO_2^+(^1\Sigma_g^+) + Rg(^1S) \rightarrow NO^+(^1\Sigma) + RgO$$
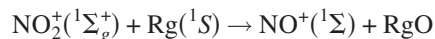
(labeled RgO).

For reasons discussed below, the only case where RgO production is probably significant is Kr, and even there the trajectory results suggest that the NO$^+$ signal is dominated by CID.
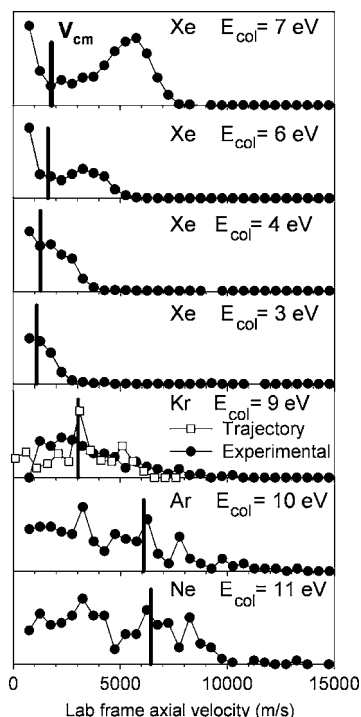
FIG. 2. Experimental and trajectory axial velocity distributions for NO$^+$ product ions at selected collision energies. Vertical lines indicate the velocity of the center of mass in the laboratory frame ($V_{c.m.}$).

The absolute cross section uncertainty is mainly a function of the collection efficiency for the NO$_2^+$ primary beam, relative to that for NO$^+$ products, which may be much slower and scattered to large angles in the laboratory frame. We estimate that the absolute error could be as large as a factor of 2 and probably varies significantly between the different systems because both kinematics and E_{col} ranges of interest are quite different. For our purposes, the more important issue is the relative error, i.e., the uncertainty in comparing cross sections for different vibrational states or collision energies, for a single rare gas partner. For Xe, the relative uncertainty is estimated to be ~10% of the cross section value (see error bars), but for the lighter rare gases, lower signal levels increase uncertainty to ~20%, as estimated by reproducibility.

Note that for all Rg, the cross sections at high E_{col} are vibrationally enhanced. Generally, the effects of bend overtone excitation are larger than those from symmetric stretch excitation, even though the stretch is the higher energy of the two vibrations. For Kr, there is also a significant difference between the two bend overtone states, with the $(0,2^0,0)$ state providing a larger enhancement than the $(0,2^2,0)$ state. This difference is quite interesting because the energy difference between these states is negligible (2 meV), as is the bending angular momentum in comparison to the collisional angular momentum.

B. Recoil velocity distributions

Axial velocity distributions for NO$^+$ generated by CID are given in Fig. 2 for the four rare gases at the indicated E_{col} values. "Forward" and "backward" are defined as NO$^+$ product ions with axial velocities faster or slower, respectively,

than the laboratory velocity of the center-of-mass frame ($V_{c.m.}$). Distributions were measured for all NO$_2^+$ vibrational states; however, only the ground state results are shown because there is no significant effect on recoil from reactant vibrational excitation, as expected for reasons discussed elsewhere.[22]

The figure gives results for Xe at several E_{col} values. Note several points. For Xe, and to a lesser extent for Kr, $V_{c.m.}$ is slow in the laboratory frame, and it appears that a significant fraction of the NO$^+$ product ions is backscattered in the laboratory frame. These products are reflected by the injection lens (see above) and eventually detected; however, they appear at long flight times, i.e., as apparently slow ions. In addition, slow ions are most strongly affected by stray fields and surface potentials. For these reasons, we do not show data for v_{axial} below 700 m/s. For Xe, this amounts to nearly the entire backscattered half of the distribution. It can be seen that at 3 eV, the products have v_{axial} values near $V_{c.m.}$, as required because the available energy in the product channel is small for E_{col} near threshold. With increasing energy, the peak moves to higher v_{axial} in the forward direction, indicating that substantial fraction of the available energy appears in recoil. Forward scattering at high E_{col} corresponds to CID in large impact parameter collisions, i.e., where the NO$_2^+$ grazes the Xe target, such that the dissociating fragments continue into the forward direction. Presumably there is also backscattered NO$^+$ from CID in small impact parameter collisions; however, these ions would appear with apparent velocities in the experimentally inaccessible range; thus we cannot judge the relative importance of these collisions.

For Kr, only the distribution at 9 eV is shown to allow comparison with the trajectory result. In general, the trajectory distribution is in reasonable agreement with experiment, although the trajectories give somewhat lower intensity of backscattered NO$^+$. Because of experimental problems with slow ions (see above) and the statistical uncertainties from the small number of trajectories, this small discrepancy is probably not significant. For Ar and Ne, the cross sections increase very slowly with E_{col}, and we show v_{axial} distributions only at the highest energies studied. At these energies, the distributions are broad and slightly backward peaked with respect to $V_{c.m.}$. The breadth indicates that there is considerable energy partitioned to recoil, and backward peaking suggests that small impact parameter collisions make the largest contribution to the NO$^+$ signal, as might be expected from the very small cross section.

IV. DISCUSSION

Figure 3 shows the dissociation coordinates for the lowest energy singlet and triplet states of NO$_2^+$. For the dissociation asymptotes, we show both values calculated at the QCISD(T)/cc-pVTZ level of theory and experimental energies, which for comparison purposes have had the ZPE subtracted out. The $^3B_2$ state energy and the barrier stabilizing it with respect to the ^3P dissociation limit were taken from the calculations of Hirst,[23] at the MR-CI/VTZ level of theory. For reasons discussed below, the triplet barrier height is unimportant in our analysis. In Hirst's paper, dissociation was
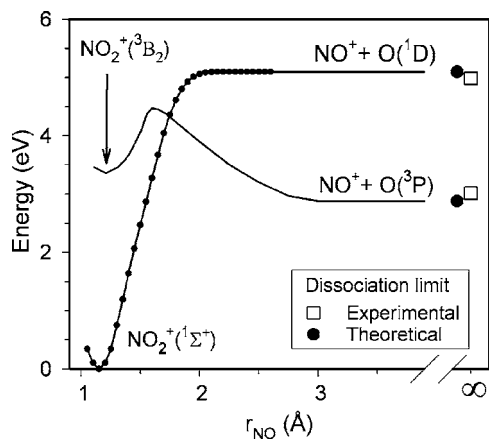
FIG. 3. Dissociation coordinate for the ground and first excited electronic states of NO$_2^+$. Points at $r_{NO}=\infty$ are the experimental and *ab initio* dissociation asymptotes.

FIG. 4. Integral cross section for CID of NO$_2^+$ with Xe plotted against total energy (E_{tot}).

examined by fixing one NO bond at a constant distance (1.22 Å, compared to 1.12 Å in NO$_2^+$) and calculating the energy as the other NO bond was stretched, keeping the geometry linear. For dissociation of the ground $^1\Sigma_g^+$ state to the spin-allowed O(^{1}D) channel, there was an apparent barrier $\sim$0.4 eV in excess of the dissociation limit. For interpretation of our Kr results, it is important to know whether this barrier is real or an artifact of having frozen the NO geometry in the calculation. To test this point, we carried out a similar singlet state dissociation coordinate calculation at the QCISD(T)/cc-pVTZ level of theory, with one bond fixed at 1.116 Å, and also found a barrier $\sim$0.2 eV in excess of the asymptotic energy when the other NO bond is stretched to $\sim$2.0 Å. We then scanned the singlet potential energy surface in the vicinity of the apparent barrier at the QCISD(T)/cc-pVTZ level of theory to examine the effect of relaxing the NO geometry. We found that allowing the nondissociating NO bond length to relax to 1.08 Å removed the barrier. This result suggests that the 0.4 eV barrier found by Hirst is largely, if not completely, an artifact of having frozen the NO geometry. The singlet dissociation coordinate shown in the figure is the minimum energy path from our potential energy surface scan.

Because xenon results in qualitatively different dissociation behavior than that of the lighter rare gases, it will be discussed first. Krypton will also be discussed separately because its behavior is quite different from that for argon and neon, and because trajectory analysis was carried out. Argon and neon have similar behavior and will be discussed last.

A. Xe

As shown in Fig. 1, collisions with Xe lead to appearance of NO$^+$ close to the lowest energy ^{3}P limit, and the cross section increases rapidly with E_{col}, reaching $\sim$65% of $\sigma_{hard\ sphere}$ by 9 eV. We are particularly interested in the near-threshold energy dependence of σ_{CID} and the relative effects of E_{col} and E_{vib}. These data directly probe the assumptions typically made in analyzing CID energy dependence to extract bond energies, as discussed in the Introduction: (1) There is at least some probability of 100% inelastic colli-

sions, i.e., CID appears immediately at the thermodynamic threshold energy. (2) At threshold, E_{col}, E_{vib}, and rotational energy (E_{rot}) are equivalent in driving dissociation. Figure 4 plots the Xe CID cross sections as a function of $E_{tot}=E_{col}+E_{vib}$. E_{rot} is negligible in our experiments because our NO$_2^+$ is generated by photoionization of supersonically cooled NO$_2$. As Fig. 4 shows, when plotted against E_{tot}, the cross sections for NO$_2^+$ in different vibrational states appear superimposable for E_{tot} up to about 1 eV above the ^{3}P threshold energy. The fits to the data shown were made within the assumptions outlined above, i.e., E_0 was fixed at the ^{3}P asymptotic energy, and E_{vib} and E_{col} were given equal effectiveness at driving CID at threshold. The best fit n parameters for the four vibrational states are all in the range from 1.7 to 1.9. No significant fit improvement results from allowing E_0 or the relative effectiveness of E_{vib} to vary, i.e., for Xe, the two assumptions are valid within our experimental error.
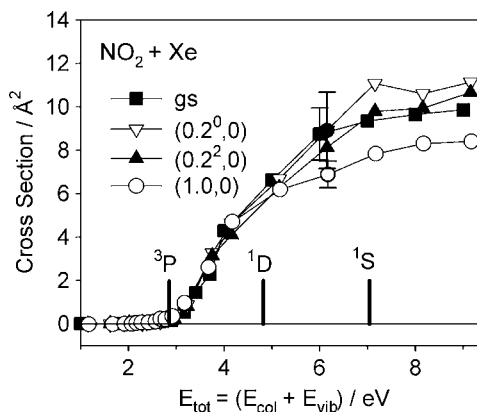
In thinking about the energetics for NO$^+$ production, the other channel that must be considered is NO$^+$+RgO. Langhoff[24] has calculated the bond energies of all the RgO in both the ground $^3\Pi$ and first excited $^1\Sigma^+$ states. For all the rare gases, the triplet Rg–O potential is repulsive; therefore we need not consider a contribution from NO$^+$+triplet XeO to the NO$^+$ signal. XeO ($^1\Sigma^+$) is calculated to be bound by 0.65 eV relative to Xe+O(^{1}D), but that still puts this channel at 4.17 eV, i.e., too far above the NO$^+$+O(^{3}P)+Xe limit to affect the threshold analysis.

While vibration and E_{col} are equivalent for Xe near threshold, Fig. 4 shows that at higher energies, there is a slight enhancement in σ_{CID} from bend overtone excitation and a slight inhibition from symmetric stretch excitation. The fact that the vibrational dependence is different at high energies compared to that at the threshold region is not unreasonable. The threshold behavior is sensitive only to that exceptional fraction of collisions that results in near 100% collision energy to internal energy ($T \rightarrow E_{internal}$) conversion, whereas the cross section magnitude at high E_{col} is sensitive to a larger fraction of the collisions, where only moderate $T \rightarrow E_{internal}$ conversion is required. In previous studies of vibrationally selected CID [H$_2$CO$^+$+Rg (Refs. 4 and 13) and OCS$^+$+Rg (Ref. 25)] vibrational excitation always enhanced

TABLE I. Fitted CID thresholds (eV) for the CID cross sections.

	gs	$(0,2^2,0)$	$(0,2^0,0)$	$(1,0,0)$
Xenon	2.85	2.85	2.85	2.85
Krypton	5.5	4.7	4.8	5.8
Argon	8.9	7.7	7.8	8.1
Neon	8.1	7.6	7.9	8.0

CID at high collision energies. The rationale was that having some E_{vib} in the reactant ions reduces the amount of $T \rightarrow E_{internal}$ conversion required for dissociation, and therefore enhances the CID probability. The observation for this system that symmetric stretch excitation *inhibits* CID at high energies implies that this vibration decreases the efficiency of $T \rightarrow E_{internal}$ conversion enough that this more than compensates for the higher initial internal energy of the reactants. The other interesting point is that, as with Kr, a larger enhancement is found from the $(0,2^0,0)$ state than from the $(0,2^2,0)$ state, i.e., bending angular momentum largely counteracts the enhancement from bend excitation. These vibrational effects are discussed further below, in light of the Kr trajectory results.

For Xe, the increase in CID cross section from threshold is rapid, and there is no inflection when the energy reaches the energy of either the ^1D dissociation or singlet RgO channels. The conclusion is that internal conversion to the triplet product channel is highly efficient, presumably mediated by strong spin-orbit coupling in Xe. One can imagine two mechanisms for dissociation to the triplet channel. In a sequential mechanism, collision with Xe would excite NO_2^+ to its low-lying $^3B_2$ state, with enough internal energy to dissociate to $NO^+ + O(^3P)$. This mechanism can be ruled out based on the energetics for this state calculated by Hirst.[23] As shown in Fig. 3, this state lies above the triplet dissociation limit, and thus cannot contribute to dissociation in the threshold energy range. Instead, the dissociation mechanism must be concerted, i.e., Xe must remain in close proximity to NO_2^+ as it dissociates, "catalyzing" access to the triplet channel with no activation energy in excess of the asymptote.

B. Kr

For Kr, the appearance energy for NO^+ from ground vibrational state NO_2^+ is ≥ 5 eV, i.e., there is no dissociation signal for energies near the ^3P dissociation limit, as shown in Fig. 1. The implication is either that spin-orbit coupling in Kr is too weak to break the spin conservation propensity rule or that the NO_2^+–Kr interaction is too weak for Kr to affect the electronic behavior of the NO_2^+ dissociation. As will be shown below, the latter assumption is clearly not correct; thus it appears that of the rare gases studied, only Xe has strong enough spin-orbit coupling to efficiently catalyze NO_2^+ access to the triplet channel.

As discussed above, the cross sections for Kr, Ar, and Ne were fit by fixing the n parameter at the value that gave the best fit for Xe (1.8), and the extracted threshold (E_0) parameters are summarized in Table I. For Kr, note several things. For ground state NO_2^+, E_0 is ~ 0.7 eV above the asymptotic energy for the $NO^+ + O(^1D) + Kr$ channel (4.82 eV), which could result either from a barrier to dissociation or from breakdown of the assumption that at least some collisions near threshold result in 100% $T \rightarrow E_{internal}$ conversion. In fact, the experiments rule out a significant barrier, consistent with our calculations of the singlet NO_2^+ dissociation coordinate (Fig. 3). If a barrier were the cause of the high ground state E_0 value, then the E_0 values for vibrationally excited NO_2^+ could shift to lower E_{col} by no more than E_{vib} for the selected state. Instead, the E_0 parameters for bend overtone-excited NO_2^+ are shifted to lower energy by more than three times the E_{vib}. Therefore we conclude that collisional $T \rightarrow E_{internal}$ conversion is inefficient for Kr, i.e., there are no collisions with 100% $T \rightarrow E_{internal}$ conversion near threshold.

A complication for the Kr system, but one that reinforces the idea of inefficient $T \rightarrow E_{internal}$ conversion, is the RgO channel. For Kr, this channel should have a threshold energy below that for CID:

$$NO_2^+ + Kr \rightarrow NO^+ + KrO(^1\Sigma^+), \quad \Delta H = 4.26 \text{ eV}.$$

The energetics for this channel are based on a singlet KrO binding energy calculated by Langhoff (0.26 eV),[24] and the endoergicity would be even lower if we used our QCISD/cc-pVTZ calculated binding energy (0.56 eV). Langhoff's calculations suggest that this reaction probably is barrierless; therefore the absence of NO^+ signal until $E_{col} \approx 5.5$ eV for ground state NO_2^+ is further evidence for inefficient collisional energy transfer for Kr.

A final point in this regard is that by using larger values of the n (threshold curvature) parameter, the $NO_2^+ + Kr$ data could be fitted to lower E_0 values, including E_0 equal to the ^1D dissociation limit or E_0 equal to the KrO threshold energy. It should be noted, however, that using large n values is simply another (and in our opinion, less transparent) way of expressing the observation that $T \rightarrow E_{internal}$ conversion is inefficient in this system.

The other interesting observation is that the vibrational effects on NO^+ production are strong and mode specific. As noted, bend overtone excitation shifts E_0 by more than three times the vibrational energy. The implication is that bend excitation enhances the probability for collisions with large $T \rightarrow E_{internal}$ conversion. In contrast, symmetric stretch excitation actually increases E_0 (the effect is also clear in the raw appearance energies). At higher E_{col}, both symmetric stretch and bend overtone excitation enhance reaction, and the effect of stretching approaches that from bending at the highest energies. This change from inhibition to enhancement for the stretch implies that, while large $T \rightarrow E_{internal}$ conversion is inhibited, the more modest conversion required for NO^+ production at high energies is enhanced. Both bending and stretching modes enhance NO^+ production more than the equivalent additions of E_{col}. For example, in the E_{col} range between 6 and 7 eV, bend overtone excitation more than triples the cross section, the higher energy symmetric stretch excitation provides a rough doubling, whereas equivalent additions of E_{col} only increase the ground state cross section by $\sim 10\% - 15\%$.

There are two obvious mechanisms by which reactant vibration can influence endoergic reactions, such as CID. To drive such reactions $T \rightarrow E_{internal}$ conversion is needed, and
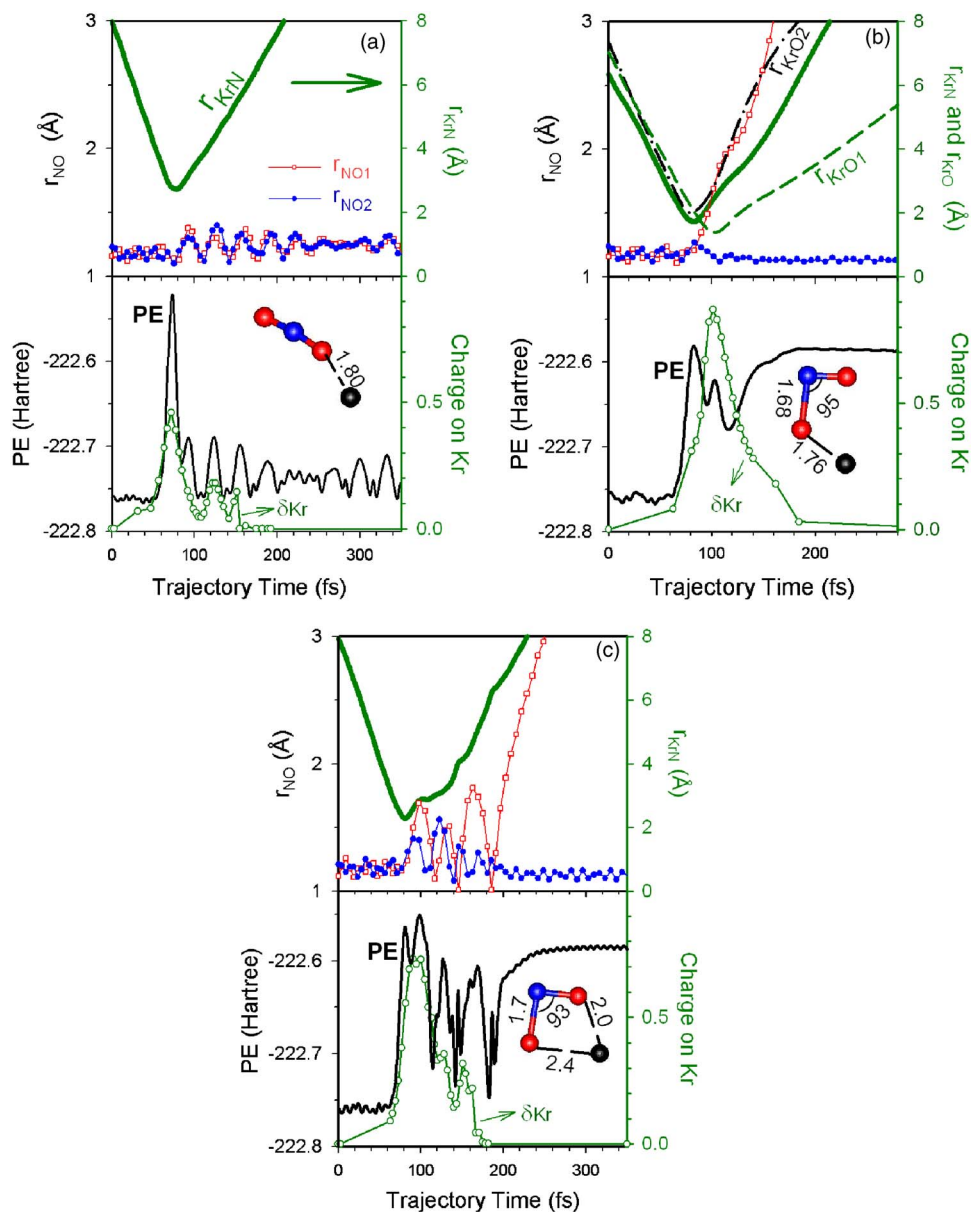
FIG. 5. Representative trajectories for NO$_2^+$ with Kr:(a) nonreactive, (b) direct-concerted dissociation, and (c) sequential dissociation. The top frame in each set shows variations in bond lengths, including r_{KrN}, r_{KrO_1}, r_{KrO_2}, r_{NO_1}, and r_{NO_2}, as appropriate. The bottom frames show the variation in potential energy (PE) and in Kr Mulliken charge (δ_{Kr}) during the trajectory. The structures show the geometry of the collision complex at the point of maximum Kr charge.

E_{vib} is expected to be the most effective form of internal energy. In that case, one might expect that increasing reactant E_{vib} would increase reaction efficiency, by reducing the amount of $T{\rightarrow}E_{internal}$ conversion required. This simple mechanism cannot explain the observed mode-specific effects nor the persistence of the vibrational enhancement at high E_{col}, where reactant E_{vib} makes a negligible contribution to the energy available to products. Instead, the mechanism for vibrational action must involve vibrational effects on the efficiency of $T{\rightarrow}E_{internal}$ conversion. One might imagine, for example, that collision with NO$_2^+$ that is distorted by vibrational motion could affect collision dynamics and energy conversion. The rather unexpected mechanism for the vibrational effects in this system becomes clear in light of trajectory analysis.

C. Kr trajectory results and analysis

Trajectory calculations were run for ground state NO$_2^+$ at $E_{col}=8.0$ and 9.0 eV, and at 9.0 eV for ground and vibra-

tionally excited NO$_2^+$. Trajectories representative of the three main types of collisions are shown in Figs. 5(a)–5(c). At the high values of E_{col} examined here, all NO$_2^+$+Kr collisions are direct, with a single turning point in the relative motion of the center of masses of NO$_2^+$ and Kr. For most collisions, the time during which NO$_2^+$ and Kr interact strongly is 20–40 fs as shown by the potential energy spike beginning at $t \approx 60$ fs. This time scale is comparable to the periods of the NO$_2^+$ vibrational modes. The most common trajectory type ($\sim$85%) is the direct nonreactive collision [Fig. 5(a)], where $T{\rightarrow}E_{internal}$ conversion is insufficient to drive dissociation. The balance of trajectories can be classified into two groups, with products corresponding to NO$^+$+O+Kr (CID, $\sim$12%) and NO$^+$+KrO (RgO, $\sim$3%), which both would contribute to the NO$^+$ production cross section in the experiments. The RgO branching fraction is undoubtedly exaggerated in the trajectories, because the singlet KrO bond energy (0.83 eV) calculated at the B3LYP/LanL2DZ level used in the trajectories is considerably higher than the bond energies calcu-

TABLE II. Comparison of experimental results with results of dissociative trajectories.

E_{col} (eV)	NO_2^+ State	σ (Å^2)			$\langle E_{recoil} \rangle$ (eV)[a]	$\langle E'_{vib}(NO^+) \rangle$ (eV)[a]	$\langle E'_{col}(NO^+) \rangle$ (eV)[a]
		Trajectory		Expt.	Trajectory	Trajectory	Trajectory
		Raw	Scaled				
8.0	gs	0.22 ± 0.1	$(0.51)^b$	0.51 ± 0.1	3.13 ± 0.25	0.45 ± 0.32	0.15 ± 0.07
9.0	gs	0.49 ± 0.1	(1.13)	1.09 ± 0.2	3.70 ± 0.46	0.70 ± 0.51	0.38 ± 0.31
9.0	$(0,2^0,0)$	0.75 ± 0.15	(1.74)	1.85 ± 0.2	3.94 ± 0.31	0.50 ± 0.32	0.34 ± 0.22
9.0	$(1,0,0)$	0.74 ± 0.15	(1.71)	1.70 ± 0.2	3.78 ± 0.40	0.65 ± 0.38	0.41 ± 0.27

[a]Angle bracket denote b-weighted average values. The "error limits" given for these average values are actually the full widths at half maximum of the corresponding energy distributions.
[b]The numbers in parentheses are scaled by a factor of 2.32.

lated at higher levels of theory (see above). For comparison with the experimental cross sections, the trajectory CID and RgO channels were simply added together.

A typical CID trajectory is shown in Fig. 5(b). Note that dissociation is direct but concerted. By this we mean that the ON–O bond breaks within a few femtoseconds of the turning point of the Kr–NO_2 motion (indicated by r_{KrN}), while the Kr is still close enough to be interacting strongly. Indeed, in these collisions it appears that there is temporary formation of a KrO species, indicated by the presence of deep local minima in the potential energy occurring as the ON–O bond breaks, and a short Kr–O_1 "bond" that breaks on a longer time scale than the ON–O bond. In contrast to this direct-concerted mechanism, about 10% of the dissociative trajectories represent a "direct sequential" mechanism, i.e., collisional activation of NO_2^+ with dissociation occurring only after the Kr atom has recoiled, as shown in Fig. 5(c).

In the experiment, the time between NO_2^+–Kr collisions and product detection is ~50 μs—far longer than it is feasible to integrate trajectories. For comparison with the experimental CID (i.e., NO^+ production) cross section, we need to include trajectories where the scattered NO_2^+ is still intact at trajectory termination but would ultimately dissociate. For this purpose, we assume that all E'_{vib} of the scattered NO_2^+ is effective at driving dissociation, and that a fraction of the NO_2^+ E'_{rot} also contributes. This fraction was estimated as E'_{rot} minus the height of the centrifugal barrier to dissociation, i.e., the rotational energy in excess of the amount that must go into recoil to conserve angular momentum. We then count as dissociative any trajectory where the sum of $E'_{vib}(NO_2^+)$ plus the excess E'_{rot} is greater than the zero point level of the NO^++O products (4.95 eV). It turns out that nearly all collisions that meet this criterion dissociate prior to trajectory termination, and the correction for delayed dissociation accounts for less than 4% of the total NO^+ production cross section.

1. CID reaction cross section and comparison with the experiment

We start by comparing trajectory NO^+ production cross sections with those from experiment for three different NO_2^+ initial vibrational states [the $(0,2^2,0)$ overtone state was not studied computationally]. Because we calculated trajectories at discrete b values, the trajectory cross sections are calculated using an extended closed trapezoidal approximation[26]

to the usual integral form [Eq. (1)], where $P(b)$ is the fraction of reactive trajectories at each impact parameter, i.e., the opacity function,

$$\sigma = 2\pi \int_0^{b_{max}} P(b)b\,db \approx \pi \sum_{b_i=0}^{b_{max}} [P(b_i)b_i + P(b_{i+1})b_{i+1}]$$
$$\times (b_{i+1} - b_i). \tag{1}$$

The maximum b at which dissociation is observed (b_{max}) is 1.5 Å for ground state NO_2^+ and 2.0 Å for vibrationally excited NO_2^+. For comparison, the orientation-averaged hard-sphere collision radius is around 2.5 Å, and the line-of-centers (LOC) model[27] predicts that the maximum b for dissociation (b_{crit}) is 1.6–1.8 Å for E_{col}=8.0–9.0 eV. The trajectory b_{max} values are thus close to those predicted by the simple LOC model. A similar relationship between b_{max} and b_{crit} was found for CID of H_2CO^+ with Ne.[13]

Table II compares the trajectory reaction cross sections with the experimental results. The calculated error limits for the trajectory values are the usual statistical uncertainties based on the number of reactive trajectories and total trajectories for each initial condition, while the experimental uncertainties are as defined above. The absolute cross sections from the trajectory results are systematically smaller than the absolute experimental cross sections: $\sigma_{traj}/\sigma_{exp}$=0.43±0.01. This disagreement in absolute scale in not surprising, given the limitations of the QCT method and the B3LYP/LanL2DZ force calculations and the substantial experimental absolute uncertainties associated with different collection efficiencies for reactant and product ions.

Whatever the source(s) of the discrepancy in absolute scale, the more important question is how well the trajectories reproduce the relative cross sections, i.e., the observed effects of changing E_{col} or NO_2^+ vibrational state. By this measure, the agreement is excellent, as shown in Fig. 6 and the scaled cross sections in Table II. The near-perfect agreement suggests that the trajectories capture the physics necessary to recover both E_{col} and vibrational effects, and should be useful in interpreting mechanistic details. The fact that the agreement is better than that expected from experimental and trajectory uncertainty limits is a result of designing both experimental and trajectory protocols to maximize error cancellation. The experimental absolute error sources, such as ion collection efficiency and gas pressure calibration, cancel in comparing data for different initial conditions. The major
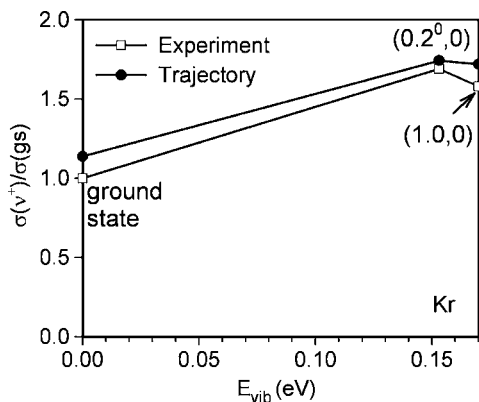
FIG. 6. Comparison of (scaled) trajectory and experimental cross sections for NO$_2^+$+Kr CID cross section at E_{col}=9.0 eV.

source of trajectory uncertainty is simply the small number of trajectories for each impact parameter and vibrational state. As discussed previously,[14] we run each batch of trajectories with identical pseudorandom sets of initial orientations, rotational energies, vibrational phases, etc. As a consequence, error resulting from inadequate initial condition sampling largely cancels in ratios of cross sections, because only the dynamical parameter of interest is varied between different sets of trajectories.

2. Energy transfer and CID dynamics

Effects of impact parameter. From Eq. (1), it can be seen that the increase in cross section with increased E_{col} and E_{vib} could result from increases in the magnitude of $P(b)$, or in the b range over which $P(b)$ is significant, or both. For ground state NO$_2^+$ at 9 eV, $P(b)$ is found to be approximately constant for b up to 0.5 Å, then falls off linearly with increasing b, with no reactive collisions observed past 1.5 Å. While this b_{max} is close to the b_{crit} value for the LOC model, the $P(b)$ peak magnitude is only 0.13 (1.0 for the LOC model), and the falloff is gradual, not sharp. Changing E_{col} from 8.0 to 9.0 eV has no effect on the shape of $P(b)$ and simply increases the magnitude. In contrast, excitation of the NO$_2^+$ $2\nu_2^+$ and ν_1^+ modes has a disproportionate effect on $P(b)$ at large b. Because the cross section scales like $P(b) \times b$, the result is substantial enhancement of the cross section.

Table II also summarizes the average product energy partitioning *for dissociative trajectories* (angle brackets denote an average value). Most of the available energy ($\sim 80\%$) is partitioned to product recoil energy, $\langle E_{recoil} \rangle$ (three body), with the balance partitioned mostly to the product ion NO$^+$ vibrational energy, $\langle E'_{vib}(NO^+) \rangle$ with lesser amounts of NO$^+$ rotational energy, $\langle E'_{rot}(NO^+) \rangle$, $\langle E'_{vib}(NO^+) \rangle$ decreases with increasing b, presumably because large b collisions have more energy tied up in orbital motion, with less along the line of centers where they can drive $T \rightarrow V$ conversion. $\langle E'_{rot}(NO^+) \rangle$ increases slowly from b=0.1 Å, peaks at b=1.0 Å, then quickly drops at larger b. This behavior is expected, because both the collision moment arm and orbital angular momentum increase with b; however, the interaction strength decreases with b. The total fractions of E_{col} con-

verted to internal energy are 61% and 58% at E_{col}=8.0 and 9.0 eV, respectively.

As might be expected, increasing E_{col} leads to increasing product recoil, vibrational, and rotational energies. Somewhat surprisingly, reactant vibrational excitation actually leads to lower $\langle E'_{vib}(NO^+) \rangle$, with significantly higher three body recoil energy. This effect may reflect the fact that vibrational excitation preferentially enhances dissociation at large b where the orbital angular momentum is large. There is, therefore, a large centrifugal barrier to product separation in such collisions, and this barrier energy converts to E_{recoil} in the products.

To put the small fraction of CID collisions in the perspective of the total scattering mechanism, it is useful to consider the distribution of $E'_{vib}(NO_2^+)$, i.e., the vibrational energy of the scattered NO$_2^+$, including both dissociate and nondissociative trajectories. For the dissociative trajectories, $E'_{vib}(NO_2^+)$ is taken as the sum of $E'_{vib}(NO^+)$ plus the NO$_2^+$ dissociation energy, i.e., the vibrational energy NO$_2^+$ *would have had* if dissociation had not occurred prior to trajectory termination. Figure 7 shows the $E'_{vib}(NO_2^+)$ distributions for each reactant vibrational state at E_{col}=9.0 eV, for different impact parameters. Results are also shown for ground state NO$_2^+$ at E_{col}=8 eV. The dissociation energy E_0 is indicated with arrows in the plots.

These distributions show an interesting effect. As noted, CID occurs in collisions with atypically large $T \rightarrow E_{internal}$ conversion, such that $E'_{vib}(NO_2^+)$ exceeds E_0. One might expect that these collisions simply correspond to the high energy tail of the $E'_{vib}(NO_2^+)$ distribution, and indeed, such behavior was observed in our previous trajectory study of CID of H$_2$CO$^+$ in collision with Ne.[13] In that system the E'_{vib} distributions decreased monotonically at high E'_{vib}. For NO$_2^+$+Kr, in contrast, the distributions are bimodal. The main component of each distribution peaks below 2 eV and decays to nearly zero below the dissociation threshold. If CID represented only the high energy tail of this main component, the cross section would be much smaller than is observed. Instead, nearly all CID results from a second component in the $E'_{vib}(NO_2^+)$ distributions, peaking above E_0. The implication is that dissociative and nondissociative trajectories are mechanistically distinct in some fashion.

Dependence on collision orientation. One of the principal motivations for doing trajectory calculations is to explore the effects of reaction dynamics that are not experimentally accessible. The relative geometry of NO$_2^+$ and Kr at the beginning of the collision is a factor that might be expected to have an effect on energy transfer, and thereby on CID probability. We want to sample the geometry at a "collision point" that is late enough that there is no time for significant geometry change before "impact" but early enough that collisional geometry perturbations are small. Consider the potential energy (PE) plots in Fig. 5. During reactant approach, the PE fluctuates due to vibrational motion of the NO$_2^+$. For our "collision point," we chose the trajectory point where the PE first deviates from the average reactant PE by more than twice the amplitude of the vibrational fluctuations. Trajectory visualization indicates that no significant distortions have occurred at this point. In large b collisions, where the NO$_2^+$–Kr
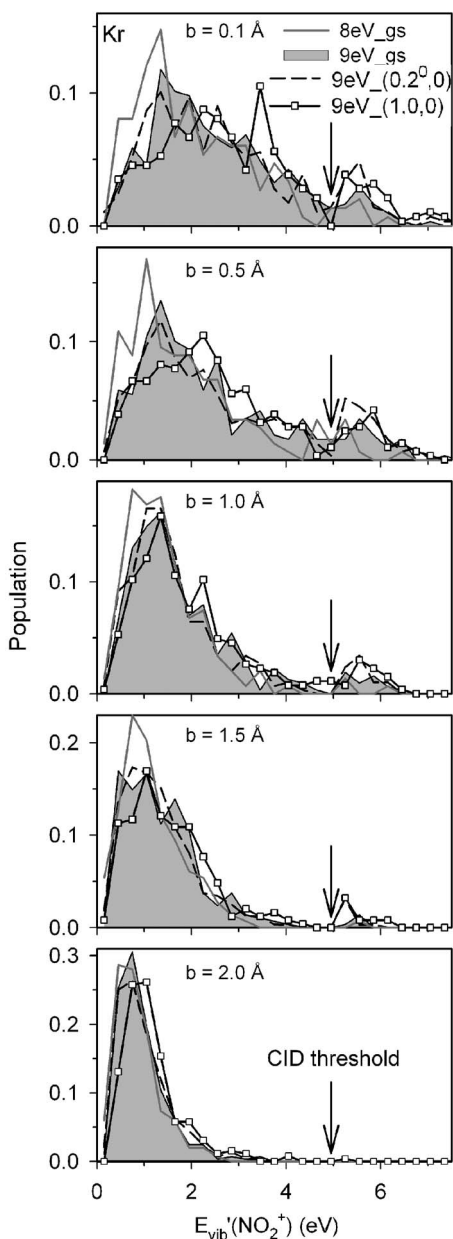
FIG. 7. Scattered NO_2^+ vibrational energy distribution following collision with Kr at various impact parameters for different collision energies and NO_2^+ vibrational states. For dissociative trajectories, $E'_{vib}(NO_2^+)$ was taken as the sum of $E'_{vib}(NO^+)$ and the NO_2^+ dissociation energy. The arrow indicates the threshold energy for CID.

interaction in never strong enough to satisfy this criterion, the collision point is taken as the point of closest approach of Kr to one of the NO_2 atoms.

One collision geometry parameter of interest is α_{Kr-O-N}, defined as the angle between Kr and the NO bond that is closer to Kr. This angle describes which atoms Kr interacts with most strongly: $\alpha_{Kr-O-N} \geqslant 90°$ corresponds to impacting the nearest O atom, while $\alpha_{Kr-O-N} < 90°$ corresponds to approaching either the center of the N–O bond or the N atom. Since vibrating NO_2^+ has negligible chance of being linear at the collision point, another parameter of interest is the dihedral angle $\Phi_{Kr-O-N-O}$, i.e., the approach angle of Kr with respect to the NO_2^+ molecular plane. Because NO_2^+ and Kr have random initial orientations, the probability of colliding

with particular values of these parameters is independent of $\Phi_{Kr-O-N-O}$ and proportional to $\sin(\alpha_{Kr-O-N})$, with the exception that $\alpha_{Kr-O-N} < \sim 45°$ is impossible because that corresponds to switching the nearest O atom in the definition of α_{Kr-O-N}. Our trajectory results show that CID probability depends strongly on both angles, with CID occurring mainly for $\alpha_{Kr-O-N} = 90° - 110°$ and $\Phi_{Kr-O-N-O} = 0° - 10°$, i.e., for collisions with Kr impacting primarily on one O atom and in the NO_2^+ plane. The orientation dependence does not change significantly with NO_2^+ initial vibrational state.

The fact that the $P(b)$ distributions go to zero near the b_{crit} value predicted by the LOC model suggests that this model has some validity here. On the other hand, the trajectory $P(b)$ magnitudes are considerably smaller than unity (the LOC value) and decrease gradually with b rather than have a sharp cutoff. The small $P(b)$ magnitudes can clearly be explained by the strong orientation dependence of CID probability—the collision must have correct orientation, in addition to sufficient LOC energy. The gradual falloff in $P(b)$ with increasing b can be related to the observation that this orientation dependence sharpens with increasing b, i.e., the reactive range of α_{Kr-O-N} narrows at large b.

Vibrational enhancement. As shown in Table II and Fig. 6, both experiment and trajectories find that excitation of the NO_2^+ $2\nu_2^+$ and ν_1^+ vibrations enhances the CID cross section by $\sim 50\%$ at $E_{col} = 9$ eV, even though these vibrations increase the available energy by less than 2%. The effect is mode specific, i.e., the lower energy $2\nu_2^+$ state generates the larger enhancement. As shown in the experimental results, the effect is even more specific at lower E_{col}, with the ν_1^+ excitation having essentially no effect near threshold and $2\nu_2^+$ excitation resulting in much larger enhancements than equivalent amounts of E_{col}. The observation of mode specificity implies that the reactant vibrational mode has a strong influence on the efficiency of $T \rightarrow E_{vib}$ conversion.

In thinking about mechanisms for vibrational effects on $T \rightarrow E_{vib}$ conversion, there are two physical limits. If the collision time scale is short compared to the vibrational period(s), then each collision takes place at fixed vibrational phase, and any vibrational effects must result from vibration-induced NO_2^+ distortion. If the collisions are much slower than the vibrational time scale, then the collisions average over the vibrational distortions but may be affected by the vibrational velocities of the atoms in the reactant molecule. For $NO_2^+ + Kr$ at $E_{col} = 9.0$ eV, the collision time scale, as judged by the potential energy surface (PES) spikes in Fig. 5, for example, is on the order of 20–50 fs, which corresponds to 2–5 Å of relative motion at the collision velocity. This time scale is comparable to the classical vibrational periods associated with the NO_2^+ modes excited ($\nu_2^+ = 60$ fs, $\nu_1^+ = 26$ fs); thus we might expect that both "distortion" and "vibrational velocity" effects might be important in controlling the efficiency of $T \rightarrow E_{vib}$ transfer.

The two modes for which substantial effects were measured are the bend ($2\nu_2^+$) and the symmetric stretch. Therefore we attempted to understand the effects in terms of distortion along the appropriate coordinates, i.e., the NO_2^+ bend angle α_{O-N-O}, and the sum of the two N–O bond lengths, Σr_{NO}. We first calculated the "geometry distributions," i.e.,
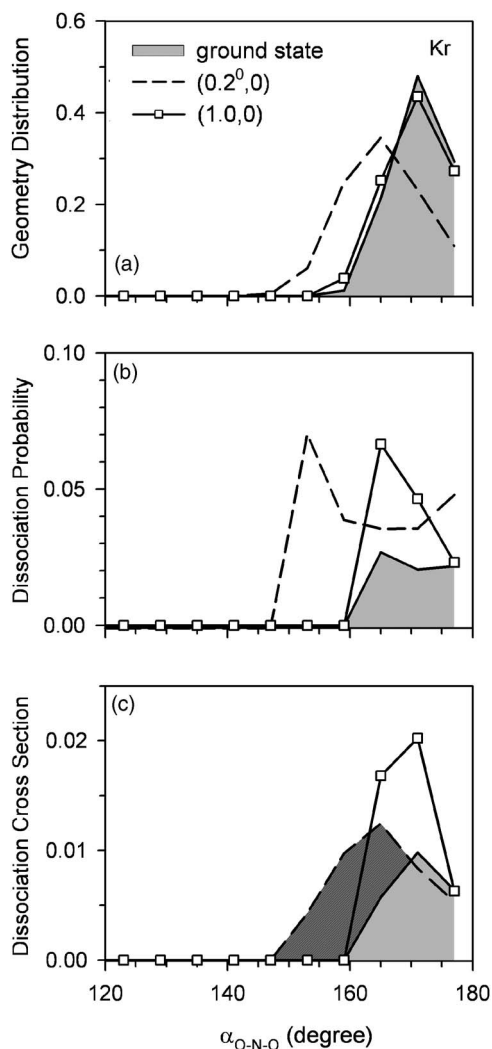
FIG. 8. (a) Probability of NO$_2^+$ being bent in different ranges of α_{O-N-O} (the angle between Kr and the NO bond that is closer to Kr) at the collision point. (b) Dissociation probability for NO$_2^+$ as a function of the value of α_{O-N-O} at the collision point. (c) Contribution of each α_{O-N-O} range to the NO$_2^+$ dissociation cross section.

FIG. 9. (a) Probability of NO$_2^+$ having different ranges of NO stretching distortion at its collision point with Kr. (b) Dissociation probability for NO$_2^+$ as a function of Σr_{NO} (the sum of the two NO bond lengths at the collision point). (c) Contribution of each Σr_{NO} range to the NO$_2^+$ dissociation cross section.

the probabilities for having NO$_2^+$ in different ranges of these two coordinates at the collision point, including both dissociative and nondissociative trajectories. As shown in Figs. 8(a) and 9(a), the zero point level of NO$_2^+$ explores α_{O-N-O} between $\sim$165° and 180° and Σr_{NO} between 2.3 and 2.45 Å. As expected, the distributions of α_{O-N-O} and Σr_{NO} are significantly broadened by excitation of the NO$_2^+$ $2\nu_2^+$ and ν_1^+ modes, respectively. For the vibrationally excited NO$_2^+$, the distributions are clearly peaked near the classical turning points of the vibrations (only one peak is visible for the bending motion, because it is symmetric at about 180°).

Figures 8(b) and 9(b) show the corresponding dissociation probability, i.e., the fraction of trajectories leading to dissociation for each range of α_{O-N-O} and Σr_{NO}, respectively. Note that for $2\nu_2^+$ excited NO$_2^+$, the dissociation probability is substantially enhanced for collisions in strongly bent geometries (which occur only for bend-excited NO$_2^+$), but also for near-linear geometries. These two effects correspond to the distortion and vibrational velocity mechanisms discussed above. For ν_1^+-excited NO$_2^+$, the α_{O-N-O} dependence is simi-

lar to that for the ground state, but the probability is higher, reflecting effects of bond stretching, as shown in Fig. 9(b). Here again, the ν_1^+-excited NO$_2^+$ has increased dissociation probability both for extended NO bond lengths (distortion) and near the equilibrium bond length (vibrational velocity).

Figures 8(c) and 9(c) show the product of the geometry distributions and the dissociation probability for each range of α_{O-N-O} or Σr_{NO}, i.e., the contribution of collisions in each range of α_{O-N-O} or Σr_{NO} to the CID cross section. Note that for $2\nu_2^+$-excited NO$_2^+$ [Fig. 8(c)], the enhancement comes entirely from collisions in strongly bent geometries (hatched area). Similarly, the effects of ν_1^+ excitation also come entirely from collisions at NO bond lengths significantly distorted (primarily stretched) from the ground state geometry. In both cases, the fact that the dissociation probability is higher near the ground state geometry for vibrationally excited NO$_2^+$ is canceled by the fact that the vibrationally excited NO$_2^+$ is less likely to collide in such geometries. In other words, the distortion mechanism is far more important

than the vibrational velocity mechanism, because vibrationally excited reactants spend more time near the vibrational turning points.

These results show that distortion enhances dissociation probability, but we still need a mechanism to explain how relatively small geometry changes can cause such large changes in $T \rightarrow E_{vib}$ conversion. The $E'_{vib}(NO_2^+)$ distributions in Fig. 7 indicate that CID does not simply represent some high energy tail of the $T \rightarrow E_{internal}$ conversion distribution; rather, there is something mechanistically distinct about dissociative collisions. Several possible distinguishing features became apparent in visualizing many dissociative and nondissociate trajectories. The nondissociative trajectories appear to be dominated by repulsive forces—not surprising at 9 eV collision energy. The dissociative trajectories, in contrast, commonly pass through configurations where the NO_2 moiety is strongly bent, with significant elongation of one or both NO bonds. In addition, the atomic motions suggest that there is significant attractive interaction between Kr and one or both O atoms. Typical examples are shown in Figs. 5(b) and 5(c). Note particularly that in Fig. 5(b), the r_{KrO_1} distance increases much more slowly than r_{NO_1} or r_{KrN}, i.e., the NO_1 bond breaks promptly, but the Kr atom and O_1 separate from each other relatively slowly.

Strong bending of the NO_2 moiety raises the possibility that there might be significant intracomplex charge transfer during the trajectory, because neutral NO_2 is bent at 134°. As a consequence, bending NO_2^+ decreases the energy separation between the $NO_2^+ + Kr$ and $Kr^+ + NO_2$ charge states $[\Delta IP(Kr-NO_2)=4.41$ eV]. We examined such intracomplex charge transfer question by running single point orbital population calculations at the B3LYP/LanL2dZ level for geometries sampled by about a dozen representative trajectories of different types. The results for typical trajectories are given as the Mulliken charge on the Kr atom (δ_{Kr}) in the lower frames of Figs. 5(a)–5(c). In all trajectories, the initial and final charges on Kr are zero as expected. For nondissociative trajectories [Fig. 5(a)], there is some charge delocalization during the part of the trajectory when the reactants are interacting strongly, as shown by Kr having Mulliken charge approaching 0.5. For all nondissociative trajectories examined, the peak Kr charge ranged from 0.4 to 0.5. As shown in Figs. 5(b) and 5(c), both concerted and sequential dissociative trajectories involve essentially complete intracomplex charge transfer (peak δ_{Kr} ranges between 0.8 and 0.9 for all dissociate collisions examined). This bimodal distribution of peak δ_{Kr} reinforces the conclusion that dissociative and nondissociative collisions are mechanistically distinct.

The objection that might be raised at this point is that our QCT methodology is inappropriate for this type of system. There are two potential problems. First, QCT cannot treat nonadiabatic scattering, i.e., it cannot follow charge transfer if it involves transitions between Born-Oppenheimer (BO) potential surfaces. Note, however, as discussed below, that the ground BO potential surface for $(NO_2-Kr)^+$ has regions where the electronic configuration is $NO_2^+ - Kr$, regions where there is significant charge delocalization between the collision partners, and also a region where the lowest energy electronic configuration corresponds to $Kr^+ - NO_2$. In other

words, it is possible to go from $NO_2^+ + Kr$ reactants to a collision complex with intracomplex charge transfer (i.e., to $Kr^+ - NO_2$) and then on to products ($NO^+ + Kr + O$) while remaining on the lowest energy BO surface. Of course the availability of an adiabatic scattering mechanism does not rule out nonadiabatic effects. We carried out time-dependent density functional theory (DFT) calculations at points along several trajectory paths to look for geometries where the splitting between the ground and first excited BO surfaces might be small, i.e., where nonadiabatic transitions might be expected. The *minimum* surface splitting ranges from ~2500 to 4000 cm^{-1}, and therefore nonadiabatic transitions should be negligible.

The other potential problem is that the B3LYP method used in the trajectories is inaccurate in situations where more than one electronic configuration contributes to the wave function. Clearly, a system like this where two charge states are collisionally mixed is a likely candidate for multiconfiguration wave functions. We tested for this problem by running single point CASSCF(8,8) calculations for all the geometries explored in the trajectories examined and found that the Hartree-Fock configuration is strongly dominant (coefficient >0.9), i.e., that multiconfiguration wave functions are not an issue in this system. In any case, the fact that the trajectories accurately reproduce both the E_{col} and NO_2^+ vibrational state dependence of σ_{CID} suggests that whatever problems may exist with the calculations will not affect the results.

The obvious questions are whether intracomplex charge transfer is a cause or an effect of collisions leading to dissociation, and if intracomplex charge transfer causes dissociation, why? Consideration of the trajectories and of the energetics of Kr–O bonding suggests a mechanism by which intracomplex CT appears to cause dissociation. The bond energy for KrO neutral in its singlet state is on the order of 0.5 eV (see above), and ground state triplet KrO is unbound. In contrast, KrO^+ is strongly bound. For this system, where reaction occurs on the singlet surface, the KrO^+ ground $^4\Sigma$ state is inaccessible, and the relevant state is the $^2\Sigma$. This state is bound by 4.87 eV [QCISD(T)//cc-pVTZ] with respect to $Kr^+ + O$ (^1D); thus when intracomplex charge transfer occurs, it switches on a strong bonding interaction with one or occasionally both O atoms in the NO_2 molecule, and thereby weakens the associated NO bond(s). In the concerted dissociation collisions [e.g., Fig. 5(b)], formation of the Kr–O bond results in immediate rupture of the associated NO bond, leading to nascent $KrO^+ + NO$ products. These products are ~1.4 eV higher in energy than the $NO^+ + KrO$ singlet state; thus as the products begin to separate, the charge transfers back, creating $NO^+ + KrO$ (KrO^+ product is not observed experimentally or in the trajectories). Finally, the weakly bound nascent KrO almost always dissociates, generating the CID products: $NO^+ + O + Kr$. In sequential dissociation collisions [Fig. 5(c)], the Kr–O bonding interaction simply leads to substantial extension of one or both NO bonds. When the charge transfers back as the $Kr-NO_2$ distance increases, the NO_2^+ product is left in a highly vibrationally excited state that dissociates to CID products.

The intracomplex charge-transfer-induced dissociation mechanism provides a ready explanation for why excitation
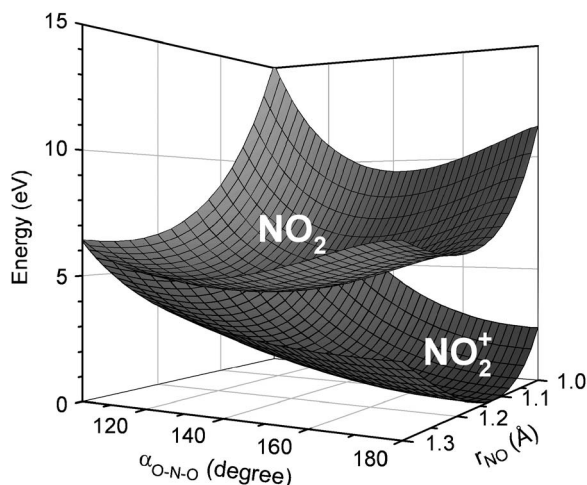
FIG. 10. B3LYP/6-311++G** potential energy surfaces for NO_2 and NO_2^+, plotted so that the difference between two surface minima equals the CT endothermicity between NO_2^+ and Kr.

of NO_2^+ bending and symmetric stretching vibrations enhances CID. Figure 10 shows the potential energy surfaces for NO_2^+ and NO_2 distortions along both the bending (α_{O-N-O}) and symmetric stretching (r_{NO}) coordinates, calculated at the B3LYP/6-311++G** level of theory. The energy scale has been adjusted so that the minima on the two surfaces differ by the difference in ionization energy between Kr and NO_2, i.e., the surface represent the situation for $(Kr+NO_2)^+$ at infinite Kr–NO_2 separation. For the linear equilibrium geometry of NO_2^+, the NO_2^++Kr surface is ~5.9 eV lower in energy than that for NO_2+Kr^+; however, both bending and symmetric stretching decrease the separation between the charge states. Kr^++NO_2 becomes the ground state for simultaneous distortions of α_{O-N-O} below ~100° and r_{NO} exceeding 1.3 Å. The situation in $(Kr-NO_2)^+$ collisions is more complicated, because forcing Kr into close proximity to NO_2 undoubtedly changes the energetics considerably; however, it is reasonable to suppose that both bending and symmetric stretching excitations would still help drive intracomplex charge transfer, and thereby enhance CID. The larger effect of bending is consistent with the fact that the relative energies of the NO_2^++Kr and NO_2+Kr^+ charge states are more strongly affected by bending than stretching, as shown in Fig. 10.

This mechanism is also consistent with the observation that the $(0,2^0,0)$ bend overtone state provides a larger enhancement than the $(0,2^2,0)$ state. For the $(0,2^0,0)$ state, all the energy goes into bending the NO_2^+, and the classical turning point has the molecule bent by ~15°. In contrast, the pseudorotating $(0,2^2,0)$ state is bent by only ~10°, albeit continuously, with the rest of the energy tied up in the pseudorotational motion. The intracomplex charge-transfer-induced dissociation mechanism requires large bending and stretching distortion of the NO_2^+ in order to couple the two charge states. It is not unreasonable, therefore, that the more strongly bent $(0,2^0,0)$ state should result in larger enhancement.

Finally, such a mechanism would explain why Ar and Ne are so much less effective and Xe more effective than Kr in

driving CID, and why Xe shows weaker vibrational effects. For Ar and Ne, the Rg^++NO_2 charge state is simply too high in energy for significant mixing, even in high energy collisions. Xe has even lower ionization energy (12.13 eV) than Kr (13.99 eV), which should enhance charge state coupling, and therefore the importance of the intracomplex charge-transfer-induced dissociation mechanism. Intracomplex charge transfer during collision implies strong electronic interaction between NO_2 and Xe, and that probably explains why transition to the ground state triplet dissociation channel is so efficient for Xe. Higher efficiency, in turn, presumably explains why vibrational effects are weaker for Xe than Kr. The smaller energy difference between the NO_2^++Xe and Xe^++NO_2 charge states means that less NO_2^+ distortion is required to allow intracomplex charge transfer, increasing CID efficiency for the ground state and leaving less room for vibrational enhancement. It should be noted that coupling between intracomplex charge transfer and CID was also observed for the O_2^++Ar system by Dressler et al.[28]

D. Ar and Ne

For Xe and Kr, CID sets in at or near the asymptotic product channel energy, implying that a significant fraction of collisions converts all or most of E_{col} to $E_{internal}$. For Ar and Ne, CID is not observed until E_{col} is nearly twice the singlet state asymptote, implying much less efficient $T \rightarrow E_{internal}$ conversion. Presumably, the high ionization energies of Ar and Ne rule out the intracomplex charge transfer mechanism that appears to be critical for NO_2^+ CID with Kr and Xe. Even so, it is surprising that Ar and Ne are such inefficient collision partners. For example, in CID studies of systems as diverse as OCS^+,[25] N_3^+,[29] and small C_n^+,[30] Ar gave CID cross sections that rose more slowly from threshold than those of Xe, but with nearly identical appearance energies. The same is true for H_2CO^+ CID with Xe and Ne.[4] We would like to understand, therefore, why Ar and Ne are so inefficient for NO_2^+, and why Ar is less efficient than Ne.

Singlet ArO and NeO are both dissociative, and the collision dynamics for these systems at high E_{col} are expected to be governed by repulsive interactions. For high energy collisions, it is reasonable to look for a kinematic explanation for the observations. A model we will refer to as the "elastic binary collision" (EBC) model[31] treats the collision in two steps. The first is elastic scattering of the Rg atom with a single atom (e.g., a terminal O atom) of the NO_2^+. The relative energy of this recoiling "target" O atom with respect to the NO moiety is then converted into NO_2^+ internal energy. There are two factors that govern the resulting internal energy. The "binary collision energy" of the Rg–target atom system is $E_{col}\mu_{Rg-T}/\mu$, where μ_{Rg-T} is the reduced mass of Rg–target atom binary system and μ is the reduced mass of the Rg–NO_2^+ system. Assuming that Rg impacts on one of the O atoms in NO_2^+, the μ_{Rg-T}/μ ratio is 0.53 for Ar–O and 0.64 for Ne–O, i.e., this factor favors the lighter rare gas. The second factor is the recoil energy of the target O atom with respect to the NO moiety, and this factor favors heavy Rg–light target atom combinations. When momentum conservation is taken into account, it turns out that this EBC model

predicts that the NO_2^+ internal energy should be $>90\%$ of E_{col} for all four rare gases, and thus does not account for the high appearance energies observed for Ne and Ar.

It is worth noting that if we only consider the μ_{Rg-T}/μ ratio, i.e., the fraction of E_{col} associated with the binary collision between Rg and the target atom, we can calculate a "binary threshold," $E_B = E_0 \mu_{Rg-T}/\mu$. Assuming that the target atom is oxygen, then E_B are 7.6, 9.0, 10.6, and 11.5 eV for Ne, Ar, Kr, and Xe, respectively. While the values for Kr and Xe are far from the experimental appearance energies (Table I), those for Ar and Ne are in reasonable agreement with experiment; thus it is tempting to propose that this binary collision energy somehow controls the final NO_2^+ internal energy. For example, one might imagine that the initial Rg–target atom collision is completely inelastic, and that this binary collision energy is then transferred to NO_2^+ in a subsequent interaction between the O atom and the NO moiety. It is important to note, however, that to conserve linear momentum in such an "inelastic binary collision" mechanism, the final $NO_2^+ E_{internal}$ must be significantly larger than the binary collision energy. Taking momentum conservation into account, the predicted thresholds would be 5.5 and 6.2 eV for Ne and Ar, respectively—much lower than the observed appearance energies.

We carried out a partial trajectory study of $Ne-NO_2^+$ collisions that provides some insight into the collision dynamics. A full set of trajectories for all impact parameters and NO_2^+ vibrational states was completed for $E_{col}=6$ eV. In agreement with experiment, no dissociative trajectories were observed, and the average $E'_{vib}(NO_2^+)$ was only 0.8 eV. We also carried out a more limited set of ~ 300 trajectories for ground state NO_2^+ at $b=0.1$ and $E_{col}=9$ eV. Here again, no dissociative trajectories were observed, consistent with experiment in the sense that σ_{CID} is too small to expect any dissociation in 300 trajectories. The product $E'_{vib}(NO_2^+)$ distributions, in contrast to those for Kr in Fig. 7, show only monotonic decline at high $E'_{vib}(NO_2^+)$, as anticipated in the absence of the intracomplex charge transfer mechanism.

In addition, we explored the dependence of the average product $E'_{vib}(NO_2^+)$ on reactant orientation. The distribution is bimodal, with the highest $E'_{vib}(NO_2^+)$ for Ne colliding either with an O atom in collinear geometry or with the N atom in a T-shaped orientation. This result is *qualitatively* consistent with the binary collision models discussed above in the sense that they also predict that the maximum final $E'_{vib}(NO_2^+)$ should be for collisions in either collinear or T-shaped geometries. This apparent agreement is superficial, however, because regardless of collision dynamics, any other geometry will result in conversion of E_{col} to product rotation, at the expense of vibration. The final $E'_{vib}(NO_2^+)$ found in the trajectories is far lower than what would result from either the elastic or inelastic binary collision models, indicating that even 9 eV is well below the energy where binary collision models are applicable.

In the end, it is not clear why Ar and Ne are such inefficient colliders for NO_2^+. Perhaps the more interesting question is not why energy conversion is inefficient for NO_2^+ but rather why it is so efficient in some other CID systems. One possibility is that an intracomplex charge transfer mechanism

occurs in those systems, even with Ar as a collider. We note that in systems where Ar is an efficient collider [e.g., OCS^+,[25] N_3^+,[29] small C_n^+ (Ref. 30)] the corresponding neutral molecules have ionization energies above 11 eV, while systems where Ar has been shown to be inefficient (e.g., NO_2^+, VO^+)[32] correspond to molecules with substantially lower ionization energies. High ionization energies increase the likelihood that intracomplex charge transfer is energetically accessible in CID collision. We intend to carry out a trajectory study of a variety of small molecular ion collision with different rare gases to clarify this issue.

ACKNOWLEDGMENTS

[1] Y.-H. Chiu, H. Fu, J.-T. Huang, and S. L. Anderson, J. Chem. Phys. **102**, 1199 (1995).
[2] Y.-H. Chiu, H. Fu, J.-T. Huang, and S. L. Anderson, J. Chem. Phys. **105**, 3089 (1996).
[3] Y.-H. Chiu, Ph.D. thesis, State University of New York at Stony Brook, 1996.
[4] J. Liu, B. Van Devener, and S. L. Anderson, J. Chem. Phys. **116**, 5530 (2002).
[5] P. Bell, F. Aguirre, E. R. Grant, and S. T. Pratt, J. Phys. Chem. A **108**, 9645 (2004).
[6] B. Uselman, J. Liu, J. Boyle, and S. Anderson, J. Phys. Chem. **110**, 1278 (2006).
[7] W. L. Hase, K. Bolton, P. de Sainte Claire et al., VENUS99, a general chemical dynamics computer program, 1999.
[8] V. Bakken, J. M. Millam, and H. B. Schlegel, J. Chem. Phys. **111**, 8773 (1999).
[9] M. J. Frisch, G. W. Trucks, H. B. Schlegel et al., GAUSSIAN03, Revision C.01, Gaussian, Inc., Wallingford, CT, 2004.
[10] S. G. Lias, J. E. Bartmess, J. F. Liebman, J. L. Holmes, R. D. Levin, and W. G. Mallard, in *NIST Chemistry WebBook, NIST Standard Reference Database Number 69*, edited by W. G. Mallard and P. J. Linstrom (National Institute of Standards and Technology, Gaithersburg, MD 2000) (http://webbook.nist.gov).
[11] G. H. Peslherbe, H. Wang, and W. L. Hase, Adv. Chem. Phys. **105**, 171 (1999).
[12] L. Laaksonen, GOPENMOL, ESPOO, Finland, 2002 (available at www.csc.fi/gopenmol).
[13] J. Liu, K. Song, W. L. Hase, and S. L. Anderson, J. Chem. Phys. **119**, 3040 (2003).
[14] J. Liu, K. Song, W. L. Hase, and S. L. Anderson, J. Phys. Chem. A **109**, 11376 (2005).
[15] W. H. Miller, W. L. Hase, and C. L. Darling, J. Chem. Phys. **91**, 2863 (1989).
[16] A. Untch, R. Schinke, R. Cotting, and J. R. Huber, J. Chem. Phys. **99**, 9553 (1993).
[17] P. d. S. Claire and W. L. Hase, J. Phys. Chem. **100**, 8190 (1996).
[18] S. O. Meroueh, Y. Wang, and W. L. Hase, J. Phys. Chem. A **106**, 9983 (2002).
[19] L. Hanley, S. A. Ruatta, and S. L. Anderson, J. Chem. Phys. **87**, 260 (1987).
[20] P. B. Armentrout, Int. J. Mass. Spectrom. **200**, 219 (2000).

[21] P. J. Chantry, J. Chem. Phys. **55**, 2746 (1971).

[22] J. Liu, B. Uselman, B. Van Devener, and S. L. Anderson, J. Phys. Chem. A **108**, 9945 (2004).

[23] D. M. Hirst, J. Chem. Phys. **115**, 9320 (2001).

[24] S. R. Langhoff, J. Chem. Phys. **73**, 2379 (1980).

[25] B. Yang, Y. H. Chiu, H. Fu, and S. L. Anderson, J. Chem. Phys. **95**, 3275 (1991).

[26] W. H. Press, S. A. Teukolsky, W. T. Vetterling, and B. P. Flannery, *Numerical Recipes in C: The Art of Scientific Computing*, 2nd ed. (Cambridge University Press, Cambridge, 1992).

[27] R. D. Levine and R. B. Bernstein, *Molecular Reaction Dynamics and Chemical Reactivity* (Oxford University Press, New York, 1987).

[28] R. A. Dressler, Y.-H. Chiu, D. J. Levandier, and C. Y. Ng, J. Chem. Phys. **113**, 8561 (2000).

[29] C. L. Haynes, W. Freysinger, and P. B. Armentrout, Int. J. Mass Spectrom. Ion Process. **149**, 267 (1995).

[30] M. B. Sowa-Resat, P. A. Hintz, and S. L. Anderson, J. Phys. Chem. **99**, 10736 (1995).

[31] J. Bordas-Nagy and K. R. Jennings, Int. J. Mass Spectrom. Ion Process. **100**, 105 (1990).

[32] N. Aristov and P. B. Armentrout, J. Phys. Chem. **90**, 5135 (1986).